This is a repository copy of *Aqueous cold-sintering of Na0.7CoO2: A benign, facile method for the densification of Na-ion compounds*.

Aqueous cold-sintering of Na$_{0.7}$CoO$_2$: A benign, facile method for the densification of Na-ion compounds

Ademola J. Adetona [a,*], Igor Levin [b], Nicola Morley [a], Oday Hussein [a], Beatia In Siame [a], Brant Walkley [c], Derek C. Sinclair [a], Ian M. Reaney [a]

[a] *Department of Materials Science and Engineering, University of Sheffield, S1 3JD, UK*
[b] *Materials Measurement Science Division, National Institute of Standards and Technology, Gaithersburg, MD 20899, USA*
[c] *Department of Biological and Chemical Engineering, University of Sheffield, S1 3JD, UK*

ABSTRACT

The properties of the hexagonal P2 sodium cobaltate, Na$_{0.7}$CoO$_2$ (NCO) phase densified using the conventional and cold sintering methods were investigated, and we demonstrated that the cold sintering method yields NCO with a relative density of over 98 % (compared to 90 % attained after conventional sintering) while maintaining high room temperature conductivity (10^{-2} Scm^{-1}). In X-ray diffraction, the original P2-phase framework is retained regardless of the sintering process, and the magnetic properties of NCO strongly depend on the densification route. Cold-sintered samples showed a classic paramagnetic response down to 2 K, while conventionally sintered samples developed a spin-glass behaviour below 6 K. The emergence of the spin-glass state on conventionally sintered ceramics was attributed to the enhanced disorder of Co^{3+} and Co^{4+} ions. A multitude of complex superstructures associated with Na ordering was identified for both cold and conventionally sintered NCO in electron diffraction.

1. Introduction

Metal oxides (A$_x$MO$_{2+\delta}$) crystallising with layered structures are amongst the most studied and used as electrode materials in Na-ion batteries [1,2]. Sodium cobaltate, Na$_{0.7}$CoO$_2$ (NCO), has been investigated for its diverse properties, making it a material of great interest in various fields. It has been studied for its cathodic [2], thermoelectric [3], catalytic [4], magnetic [5,6], and superconducting properties [7–9]. Na$_{0.7}$CoO$_2$ has a hexagonal crystal lattice composed of layers of edge-sharing [CoO$_6$] octahedra alternating with layers of Na, as shown in Fig. 1.

Na$_x$CoO$_2$ exhibits five different phase transitions according to Lei *et al.*, Fig. 2 [10]: O3 ($x = 1.0$, *R-3 m*, $a = 2.8880$ Å and c $= 15.6019$ Å); O′3 ($x = 0.83$, *C2/m*, $a = 4.8912$ Å, $b = 2.8681$ Å and $c = 5.7937$ Å, β = 111.84°); P′3 ($x = 0.67$, *C2/m*, $a = 4.9126$ Å, $b = 2.8270$ Å and $c = 5.7087$ Å, β = 106.06°); P2 ($0.68 \leq x \leq 0.76$, *P6$_3$/mmc*, $a = 2.8320$ Å and $c = 10.8971$ Å) and P3 ($x = 0.56$, *R3m*, $a = 2.8192$ Å and $c = 16.5880$ Å). Additionally, the P′3 and O′3 phases coexist within a narrow temperature window of ≈ 283 K. The P or O (prismatic or octahedra) refer to the alkali-ion sites with the number of alkali-ions designated as 2

or 3 within the structure [11].

Na$_{0.67}$CoO$_2$ shows an oxygen evolution reaction (OER) at room temperature in an alkali solution, which is influenced by the loss of H$^+$ ions from the surface oxygen, facilitated by O–2p hybridisation and the low-spin Co^{3+}/Co^{4+} π-bonding d-states [12]. Several studies [7–9] have all reported superconducting behaviour in Na$_x$CoO$_2$ ($0.3 \leq x \leq 0.4$) at 5 K ascribed to the intercalation of H$_2$O into Na$_x$CoO$_2$ ($0.3 \leq x \leq 0.4$) accompanied by the expansion of the c-axis lattice parameter in the hexagonal (*P6$_3$/mmc*) cell from 11.16 Å to 19.5 Å. The arrangement of Na-ions differs from that in the parent compound, while the water adopts a structure reminiscent of ice.

Building on the initial work by Kähäri *et al.* [13], Randall's group at Pennsylvania State University demonstrated a reduction in ceramic sintering temperatures to < 473 K for a wide range of compositions using a methodology referred to as cold sintering (CS) [14–17]. CS is inspired by geological processes in which materials are densified in mineralised hydrothermal fluids under pressure. Cold sintering technique has been used to densify and develop (RF) radio frequency material [18], ceramics capacitors and devices [19], Bioglass® [20], and fabricate Li-ion electrodes and electrolytes (LLZAO) all below 573 K

---

* Corresponding author.
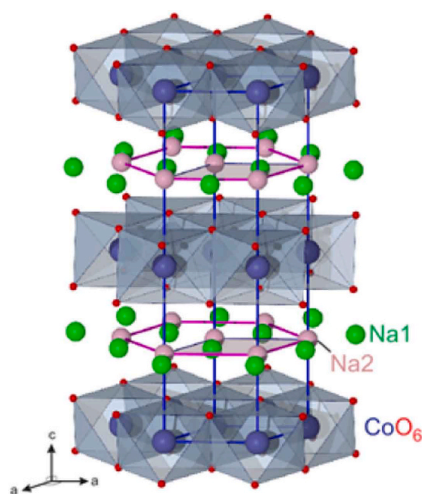*E-mail addresses:* adetonaademola077@gmail.com, ajadetona1@sheffield.ac.uk (A.J. Adetona).

Fig. 1. The crystal structure of $Na_{0.7}CoO_2$. The image displays the layered structure of Na and CoO_6, with the magnetic cobalt atoms arranged in a frustrated triangular setting [5].
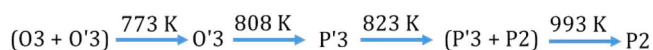

Fig. 2. The phase transition sequence of $Na_{0.7}CoO_2$ on heating [10].

[21]. CS offers not only the most significant energy reduction per capital outlay of any low-energy densification technology but also facilitates the co-sintering of dissimilar materials to form ceramic-electrode multilayers, ceramic-ceramic composites, and ceramic-polymer composites [22–25].

In this work, the aqueous CS of NCO is demonstrated, and its properties are explored. The results are compared with conventionally sintered NCO ceramics. The phase, microstructure, electrical and magnetic properties of the cold and conventionally sintered ceramics were investigated.

2. Experimental methods

2.1. Ceramic fabrication

NCO powder was sourced from the NEI Corporation and used without further processing. The NCO powder were pressed into pellets at 375 MPa using a uniaxial cold press and conventionally sintered in an Elite Thermal System Limited Furnace (BSF12/6 2416CG + 3216IAL) at 1073 K in air for 12 hours. For cold sintering, NCO powder was mixed with 25 vol% aqueous H_2O using a mortar and pestle for $\approx$ 4 minutes. During the mixing, some of the H_2O evaporated until the NCO sample became a hygroscopic salt before being transferred to a 10 mm die and pressed at various pressures (250–500 MPa) using a Specac uniaxial hot-pressed coupled with Specac Atlas Series Platen Controller at 473 K for 1 hour. The pressing duration was timed from when all parameters reached their maximum (i.e. 500 MPa and 473 K). The pressure was applied from the initiation of pressing at a heating rate of 274 K per minute. The density of the conventional and the CS NCO ceramic was measured using Archimedes' and geometric methods.

2.2. Structural and microstructural characterisation

A PANalytical[1] Aeris X-ray diffractometer (XRD) operating with Cu-Kα radiation ($\lambda = 0.154$ nm) was used to obtain diffraction data in the 2θ range 10–80°, with a step size of 0.02°. Selected samples were also measured in a Bruker D8 Discover XRD operated with Cu-Kα radiation and equipped with the Eiger2X 500 K area detector, which facilitates the texture analysis; a nickel filter was used to mitigate the cobalt fluorescence. This instrument enables sub-mm irradiated areas helpful for probing cross-sectional surfaces of sintered pellets. The average particle size distribution of the NCO green powder was measured using Malvern Mastersizer Particle Analyser 3000 with the refractive indices of the dispersant (water) and the NCO green powder taken to be 1.33 and 1.870, respectively. The NCO green powder and the sintered pellet microstructures were examined in an FEI Inspect Scanning Electron Microscope (SEM). Transmission Electron Microscopy (TEM) images and electron diffraction patterns were collected in a Titan (S)TEM (Thermo Fischer) operated at 300 kV and equipped with a OneView (Gatan) camera. Electron energy loss (EELS) and energy dispersive (EDS) spectroscopic measurements were completed in a different Titan (S)TEM operated at 300 kV and featuring an aberration-corrected and monochromated probe. EELS spectra were recorded using the outer collection angle of $\approx$ 13 mrad. The spectra were corrected for plural scattering using the low-loss spectra recorded from the same locations and the Fourier ratio method implemented in the Gatan Digital Micrograph software. The Co L_3/L_2 intensity ratio was determined using an approach outlined in [26]. EDS spectra were quantified using the Cliff-Lorimer method in HyperSpy.

2.3. Magnetic characterisation

A Quantum Design SQUID MPMS magnetometer was used to investigate the magnetic behaviour of the NCO sample. The real and imaginary parts of magnetic susceptibility were measured as a function of temperature between 2 K and 300 K at zero applied field (due to remanence on the superconducting magnet, the actual field was 0.4 Oe) for both heating and cooling cycles. A field of 100 Oe was then applied, and the measurement was repeated between 2 K and 35 K to study the low-temperature behaviour.

2.4. Impedance spectroscopy

An Oxford instrument CCC1104 closed cycle cooler Cryostat was used to probe the electrical properties. The polished surface of the NCO pellets was coated with an In-Ga electrode and allowed to dry without annealing. Due to the high conductivity of the NCO ceramics, electrical measurements were performed at sub-ambient temperature. The Cryostat was calibrated using a blank, open, and closed circuit to correct any error associated with the measurement. After the impedance (Z*) measurement, a geometric correction factor accounting for the pellet thickness and sample-electrode area (surface area normalisation) was applied to the data. Data analysis and circuit fitting were performed using ZVIEW-impedance Software version 2.4 Scribner Associates.

---

3. Results

3.1. Size distribution of the NCO green powder

The average particle size distribution of the NCO green powder was $\approx 22.7\ \mu m$ with a size uniformity of 0.7, as shown in Table S1. The NCO particle size was measured at various D_x (x =10, 50 and 90 %) values where D_x represents the diameter of the particle at a percentile (x) in the size distribution curve. The particle size distributions of the NCO powder at D_{10}, D_{50} and D_{90} are ≈ 5.3, ≈ 22.7 and $\approx 57.3\ \mu m$, respectively, as shown in Table S1.

3.2. Relative density measurement

Table 1 compares the sintered (measured using Archimedes and geometric methods) and the theoretical density of NCO ceramics, with the latter value of $4.72\ gcm^{-1}$ adopted from the literature [5], to give the relative density (measured/theoretical). CS NCO had a relative density of $98.94 \pm 2.00\ \%$ at 500 MPa and 473 K, similar to $LiCoO_2$ (LCO) densified by the same authors [27] compared to $90.89 \pm 2.00\ \%$ for the conventional NCO ceramics. Prior to selecting the CS NCO ceramic in Table 1, an optimisation study was conducted to determine the optimal combination of pressure, temperature and time for cold sintering of NCO ceramics. The study revealed that the cold-sintered NCO ceramics exhibited higher densities compared to the conventionally sintered NCO at all optimised parameters, as shown in Table 2.

3.3. Microstructure from scanning electron microscopy

Fig. 3a shows the SEM micrographs of the lightly polished surface of the conventionally sintered NCO ceramics. Some regions are well densified with grains forming triple junctions, but intergranular porosity is evident throughout the sample. The microstructure is consistent with a $\approx 90\ \%$ relative density sample. Fig. 3b depicts the lightly polished surface of NCO ceramics aqueously cold-sintered. The microstructure appears almost fully dense, with scant evidence of porosity. Samples generally react with the atmosphere (as shown in Fig. S1, supporting information), and care must be taken not to over-interpret individual features, as artefacts can readily form on exposure to the air and during grinding and polishing. The grain size of the green NCO powder, cold and conventionally sintered NCO was estimated by using the line intercept method in Image J software. The average grain/particle sizes of the green powder, cold and conventionally sintered NCO ceramics were $\approx 22.7\ \mu m$, $\approx 6.8\ \mu m$ and $\approx 9.5\ \mu m$, respectively. After sintering, the average grain size of the NCO was over 50 % smaller than the starting particle size, suggesting that the green powder was agglomerated. The average grain size in the conventionally sintered NCO was $\approx$ 30 % larger than that of the cold-sintered NCO ceramic, indicating that the cold-sintering method limits the grain growth of NCO, as observed in other cold-sintered materials [28]. The micrographs of the NCO green powder are shown in Fig. S2.

3.4. Phase composition and texture from XRD

XRD patterns of the NCO raw powder confirm a single-phase material with peaks matching P2-type $Na_{0.71}CoO_2$ (PDF N°: 00–078–2822, space group $P6_3/mmc$). XRD patterns of cold and conventionally sintered NCO powders obtained by grinding the sintered pellets are shown in Fig. 4, suggesting that the original P2-phase framework is retained regardless of the sintering process [29,30]. The only significant extra peak appears at $2\theta \approx 30.1°$. This peak, which is most noticeable in the CS sample, does not match any conceivable impurity phases but can be indexed to the presence of the O'3-like monoclinic phase, which was consistent with the phase diagram reported in [10].

Table 2
The optimisation study of the density of cold-sintered NCO.

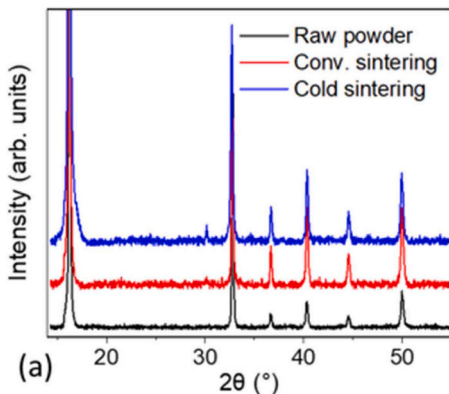|	Variable Temperature, Time and constant Pressure				Variable Pressure (MPa), Constant Temperature (473 K), and Time (60 minutes)			
	500 MPa/423 K		500 MPa/473 K		250	312	375	437
Time (minutes)	Density (g/cm³)	ρ_r (%)	Density (g/cm³)	ρ_r (%)	ρ_r (%)	ρ_r (%)	ρ_r (%)	ρ_r (%)
15	4.30	92	4.40	94	-	-	-	-
30	4.31	93	4.41	95	-	-	-	-
45	4.33	93	4.54	97	-	-	-	-
60	4.36	94	4.67	98	94	95	97	97
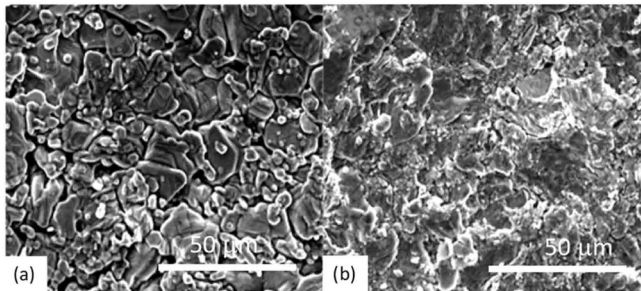
Fig. 3. SEM micrographs of NCO (a) conventionally sintered and (b) cold-sintered.

Fig. 4. XRD patterns of NCO raw powder, cold and conventional (conv). sintered NCO.

Table 1
The density of NCO is calculated using Archimedes (H_2O as the measuring fluid) and the geometric method. The uncertainty in the relative density (ρ_r) refers to a single standard deviation.

	Sintering condition			Archimedes	Geometric	Relative density
NCO	Temperature (K)	Compacted pressure of pellets before sintering (MPa)	Time (hours)	ρ / gcm^{-3}	ρ / gcm^{-3}	ρ_r (%)
Conventional	1073	375	12	4.29 ± 0.08	4.05 ± 0.05	90 ± 2
Cold sintered	473	500	1	4.67 ± 0.08	4.48 ± 0.05	98 ± 2

3.5. Structure and microstructure from transmission electron microscopy

Consistent with the XRD results, all fundamental reflections in the electron diffraction patterns from the raw NCO powder were indexed according to the hexagonal $P6_3/mmc$ structure with lattice parameters $a_0 \approx 2.8$ Å, $c_0 \approx 11$ Å. However, most grains revealed extra, weaker reflections, both sharp and diffuse, representing various superlattices reported for NCO and attributed to distinct ordered of arrangements of Na atoms. The most frequent ones observed here were those with modulations in the hexagonal plane exhibiting a periodicity with $\mathbf{k} \approx 0.125$ [110]* (asterisk denotes a reciprocal-space vector) (Fig. 5a) and $\mathbf{k} = \frac{1}{2}$ [110]* (Fig. 5b). Both superstructures develop 60° twin domains, which contribute three sets of superlattice reflections in [0001] selected area diffraction patterns. Grains with other complex patterns of diffuse spots (Fig. 5c) were also frequently observed. Even for the same type of ordering, the correlation length varied from grain to grain. Previous studies of NCO samples having controlled stoichiometry identified no clear relationship between the composition and preferred type of Na ordering; in many cases, samples with a confirmed narrow compositional spread contained several superstructures [31,34]. Nevertheless, a multitude of the Na ordering patterns observed here, which are characterised by grain-to-grain variations of the degree and spatial extent of such ordering, suggest certain compositional non-uniformity in the powder.

This plethora of superstructures was retained after both conventional and cold sintering. Despite the exposure to a significantly higher temperature, the conventionally sintered sample still contained grains featuring the diffuse superlattice spots (Fig. 5d) of the kind observed in the raw powder (Fig. 5a) and the cold-sintered samples (5 g and Fig. 6a), albeit with a different periodicity characterised by $\mathbf{k} = 1/6$[110]*. These superstructures have their ordering modulation vectors in the hexagonal {0001} plane directed at an angle (e.g., $\approx 23°$ in Fig. 5e and f and $\approx 13°$ in Fig. 5i) to the axes of the fundamental lattice. Similar types of ordering patterns with rotated axes but having somewhat different periodicity were reported in NCO [32,34]. The Fourier filtering of high-resolution TEM (HRTEM) images of these superstructures confirmed that they also exist as twin-domain variants. The conventionally sintered sample predominantly exhibited the superstructures shown in Fig. 5e and f, whereas the dominant superstructure in the cold sintered sample was that with $\mathbf{k} = \frac{1}{2}$ [110], which resembles the O′3
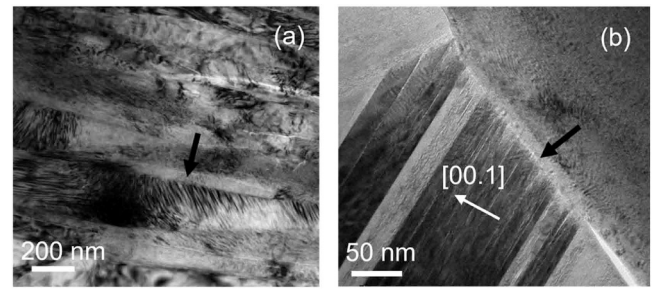

Fig. 6. Bright-field TEM images of the (a) cold-sintered and (b) conventionally sintered NCO. Grain boundaries are indicated with black arrows, and the approximate direction of the hexagonal c-axis is illustrated by the white arrow in (b).

lattice but with extinction rules relaxed (Fig. 5h). This O′3-like superstructure can account for the $2\theta \approx 30.1°$ peak which is most prominent in the CS sample. However, given the large variety of superstructures in each sample and the limited statistics afforded by TEM, we could not quantify the relative frequencies of distinct types of ordering patterns in different samples.

Like in SEM micrographs, the microstructures of the cold and conventionally sintered samples reflect their disparate densities. The cold-sintered TEM sample was prepared parallel to the surface of the initial pellet; therefore, because of the [0001] texture, preferentially exposed grain morphologies as viewed along orientations close to the c-axis. Yet, a certain fraction of the grains with the c-axis residing in the TEM sample plane were also present, revealing lamellar morphologies with cross-sectional dimensions of the order of 200 nm (Fig. 6a). These lamellae exhibited significant disorder manifested as nanoscale and mesoscale striations in diffraction-contrast images (Fig. 8a). High-resolution phase-contrast imaging of individual lamellae confirmed a sub-structure of out-of-phase domains and adjacent regions having their c-axes misoriented by several degrees (Fig. 7). The grains that were viewed along [0001] direction and thus perceived to expose surfaces of the lamellae exhibited a relatively high number density of dislocations and a sub-structure consistent with the presence of fine-scale domains and low-angle boundaries. The conventionally sintered sample, which was prepared in cross-sectional geometry, contained plate-like but more
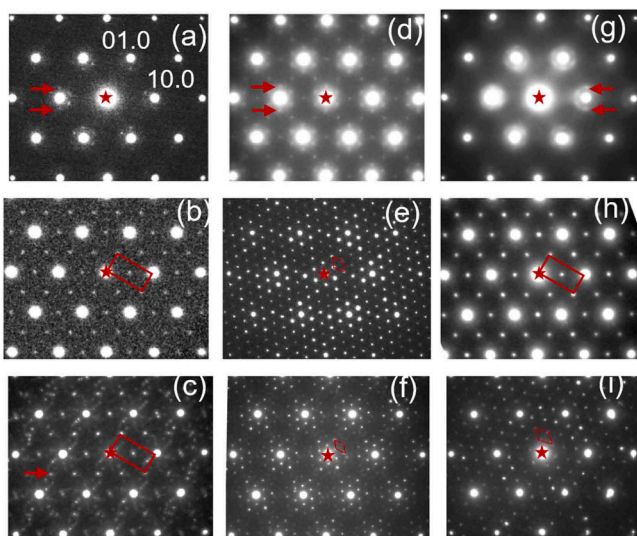

Fig. 5. Tableau of [0001] selected area electron diffraction patterns illustrating various superstructures encountered in the initial NCO powder (a-c), conventionally sintered (d-f) and cold-sintered (g-i) samples. The superstructure reflections and their repeat units are indicated using red arrows and parallelograms.
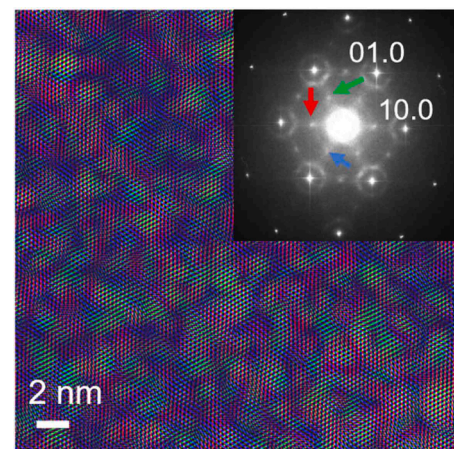

Fig. 7. RGB rendering of a sum of three images obtained via the Fourier filtering of an HRTEM image of a region in the cold-sintered sample featuring the same diffuse superlattice reflections as in Fig. 5g. Each of these images was generated using one of the three sets of superlattice spots indicated using red, green, and blue arrows in the inset, which shows the Fast Fourier Transform of the original HRTEM image. The RGB image displays distinct regions of these colours, indicating that the superstructure forms three spatially distinct 60° domains.

equiaxed grains, like in cold-sintered ceramics, displayed considerable stacking disorder along the *c*-axis and misoriented adjacent domains (Fig. 8b). In the case of conventional sintering, the stacking disorder can be attributed to the O $\leftrightarrow$ P structural transformation on cooling from the processing temperature. According to the published phase diagram, at 200 °C used for cold sintering, the sample should have resided in the O3+O3′ phase field, where the two structures differ by lattice distortions. Such a mixture in itself could account for the observed high incidence of defects. Additionally, pressure could alter phase equilibria, lowering the temperature of the O $\leftrightarrow$ P transition.

The grain boundaries in conventionally sintered NCO samples show no evidence of a secondary phase. EDS analysis revealed that the conventional samples contained a non-negligible fraction of grains having significant Na deficiency relative to the rest of the material. Additionally, in the conventional sintered NCO sample, occasional thin lamellae containing exclusively Na and O are intergrown with the NCO structure. The sporadic nature of such findings precluded definitive attribution of this secondary phase to a specific sintering route.

We used the L_3/L_2 Co white-line intensity ratio in core-loss EEL spectra to probe the oxidation state of the Co (Fig. 9a). As reported previously, this ratio decreases monotonically as the oxidation state increases [26]. However, the dependence is non-linear, flattening considerably for the oxidation states between +2.5 and +4, which reduces the reliability and accuracy of the EELS analysis in this range. Our Co L_3/L_2 ratios measured for the reference samples (≈ 4.5 for $CoNb_2O_6$, ≈ 2.4 for Co_3O_4) were close to the values published by [33] and consistent with the ratio of 2.2 ± 0.05 measured here for NCO, indicating the expected oxidation state above +3. Although we attempted to use $CoSi_2$ as a reference for Co^{4+}, the edge-like appearance of the white lines (especially L_2) in this compound introduces an ambiguity in determining their intensity ratio (here determined as $L_3/L_2 \approx 2$) if applying the procedures devised for oxides [26]. In the absence of reliable references for Co^{3+} and Co^{4+}, quantifying the oxidation state in our samples was challenging. A comparative analysis of the simultaneously recorded EELS and EDS signals from the initial NCO powder and differently sintered NCO ceramics suggested that both conventional and cold sintered NCO samples exhibited similar composition and Co oxidation state (Fig. 9b). EELS and EDS spectrum imaging (≈ 2 nm per pixel) of grain-boundary regions in the sintered samples revealed no detectable differences between the boundaries and grain interiors.

3.6. Impedance Characteristics

Complex impedance-plane, Z*, plots for conventional and cold-sintered NCO ceramics with In-Ga electrodes are shown in Fig. 10 and Fig. 11, respectively. At room temperature, both samples exhibit a single, poorly resolved arc with a high-frequency, non-zero intercept of the Z′ axis, similar to that obtained for LCO [27]. The total (dc) resistivity
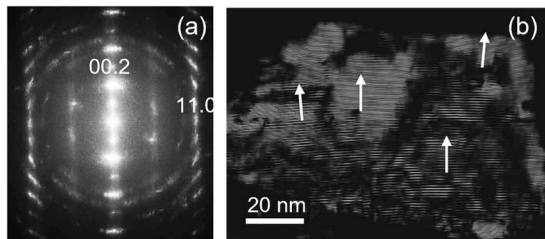

Fig. 8. (a) Fast Fourier Transform of an HRTEM image of a lamellar grain in the cold-sintered sample recorded in [11.0] orientation. A spread of *c*-axis orientations and stacking disorder in the imaged region are evident. (b) Phase-contrast image obtained as the inverse Fourier transform of (a) using 00.1 and 00.2 sets of reflections. The image reveals a high incidence of out-of-phase domains and regions, about 20 nm in size, with slightly different orientations of the *c*-axis, indicated using white arrows.
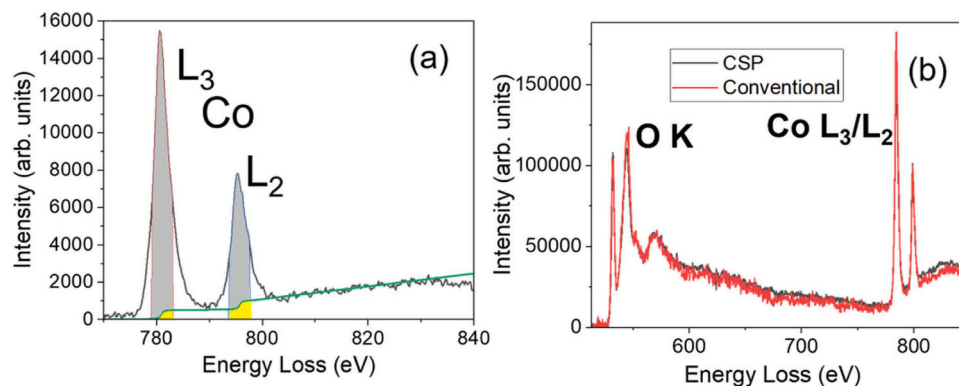
estimated from the low-frequency intercept of the arc is in the range of ≈ 40 Ωcm to 50 Ωcm, and the non-zero intercept at high frequency is between ≈ 20 Ωcm to 45 Ωcm. Changing the electrodes from In-Ga to sputtered Au removed the low-frequency arc for both samples, displaying inductive effects (i.e. positive Z″ values) with Z′ values remaining below 50 Ωcm. These results are consistent with the NCO ceramic being highly conductive at room temperature and showing signs of a superconductor, as previously reported for this ceramic [6–9]. The In-Ga electrode samples' low-frequency arc was associated with a non-ohmic electrode contact.

The Z* data in Fig. 10 and Fig. 11 were modelled using an equivalent circuit based on a single resistor connected in series with a parallel Resistor-Capacitor element. The single resistor (associated with the high frequency, non-zero intercept of the Z′ axis) is attributed to the overall resistivity of the ceramic ($R_{ceramic}$) and the parallel RC element (associated with the arc in Z*) is attributed to the electrode effect ($R_{electrode}C_{electrode}$). Performing measurements at higher temperatures was difficult for both methods due to the highly conductive nature of the NCO ceramic (Superconducting behaviour), while measurements at sub-ambient temperatures resulted in modest changes in the Z* plots: the arc in the Z* increased in magnitude with decreasing temperature, with only minor changes in the non-zero intercept, Fig. 10 and Fig. 11. According to this trend, $R_{electrode}$ increased on cooling, with $C_{electrode}$ in the range from 3 nF/cm to 15 nFcm^{-1}, whereas $R_{ceramic}$ decreased. The R values, converted into conductivity (σ) (where $\sigma = \frac{1}{R}$), are shown in Arrhenius format in Fig. 12. These plots suggest metallic-type conduction for both NCO samples and non-Arrhenius-type behaviour for the non-ohmic contacts. Due to the conductive nature of NCO, it is impossible to use impedance spectroscopy for probing the grain and grain-boundary contributions to the overall impedance response. Nevertheless, Fig. 11 demonstrates that cold-sintered NCO exhibits total conductivity values comparable to those obtained for conventionally sintered ceramics, Fig. 10. The values associated with the impedance data can be found in the supporting information Table S2 – S3.

3.7. Magnetic Properties

Due to signs of superconductivity shown during impedance measurement, we investigated the magnetic properties using a SQUID magnetometer. Fig. 13 shows the real part of the susceptibility of the cold-sintered NCO sample as a function of temperature and applied magnetic field. The susceptibility increases monotonically on cooling to 2 K, consistent with paramagnetic behaviour [5]. Further, there is no difference between the data recorded on heating and cooling of the data for different applied magnetic fields. The conventionally sintered sample also exhibited a paramagnetic behaviour down to 6 K. However, below this temperature, the susceptibility dropped before increasing again on further cooling (Fig. 14), with the peak at 6 K suggesting a change from paramagnetic to anti-ferromagnetic or spin-glass behaviour. A spin-glass state is typically characterised by a frequency dispersion in the susceptibility, confirmed by the data in Fig. 15, which reveals a peak shift as the frequency increases from 75.7 Hz to 757 Hz.

Thus, cold sintering yielded classic paramagnetic behaviour in NCO down to 2 K, whereas conventional sintering produced a sample that exhibited a paramagnetic $\rightarrow$ spin-glass transition at ≈ 6 K.

4. Conclusions

We demonstrated that cold sintering yields NCO ceramics with nearly theoretical densities, compared to 90 % achieved after conventional sintering. XRD confirmed that both methods retain a hexagonal P2-like structure irrespective of the densification process. Electron diffraction patterns recorded in TEM reveal a spectrum of different superstructures in both conventional and cold-sintered samples. The lack of significant difference in the Co^{3+}/Co^{4+} ratio suggested from the

Fig. 9. (a) Illustration of a procedure used to determine the L_3/L_2 white-line intensity ratio for Co. Blackline – experimental spectrum containing Co L_3 and L_2 lines from the cold-sintered NCO after subtracting the power-law background and removing plural scattering [26]. Green line – a double-arctan function fitted to the spectrum with the 2:1 L_2:L_3 step ratio to model the continuum background. Grey-shaded areas under the peaks – integration windows. (b) Comparison of EEL spectra containing O K and Co L_3/L_2 edges between the conventional and cold-sintered (CSP) NCO (similar thickness of about 100 nm).
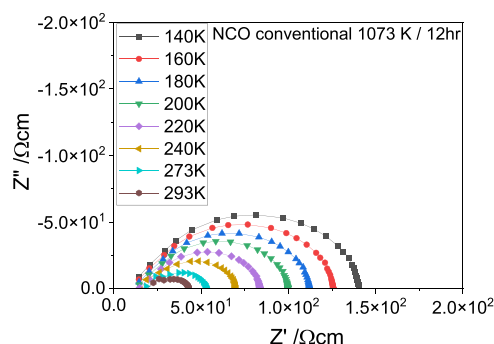

Fig. 10. Impedance (Z*) plots of the conventional sintered NCO ceramics measured between 140 K and 293 K.
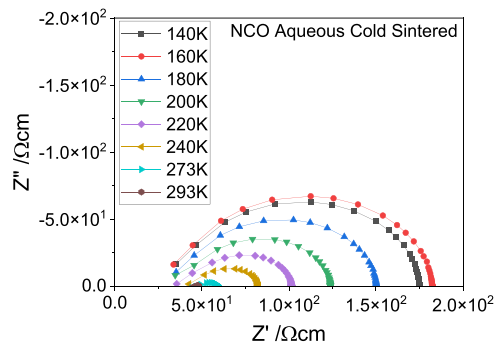

Fig. 12. Arrhenius plots of the extracted conductivity values for conventional (conv.) and cold-sintered NCO ceramics.

Fig. 11. Impedance (Z*) plots of the cold-sintered NCO ceramics measured between 140 K and 293 K.

Fig. 13. and insert: Real ac susceptibility for the cold sintered NCO as a function of temperature and applied magnetic field for an ac frequency of 757 Hz. Solid and open symbols correspond to heating and cooling, respectively.

comparison of the L_3/L_2 lines in the EELS data of the differently sintered samples indicates that the changes in this ratio are within the uncertainty of the EELS analysis. Both samples displayed a total conductivity in the range of 10^{-2} S/cm at room temperature. However, conductivity measurements at higher temperatures were challenging for both methods due to the highly conductive nature of the NCO ceramic and measurements at sub-ambient temperatures showed modest changes in the Z* plots. In addition, both methods display metallic-type conduction and non-Arrhenius-type behaviour. The SQUID Magnetometer measurements revealed that the processing route significantly affects the magnetic properties of NCO. The cold-sintered sample behaved as a classic paramagnetic on cooling from room temperature down to 2 K, whereas the conventionally sintered sample, which also exhibited a
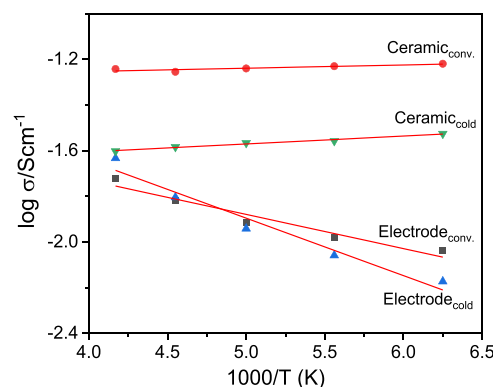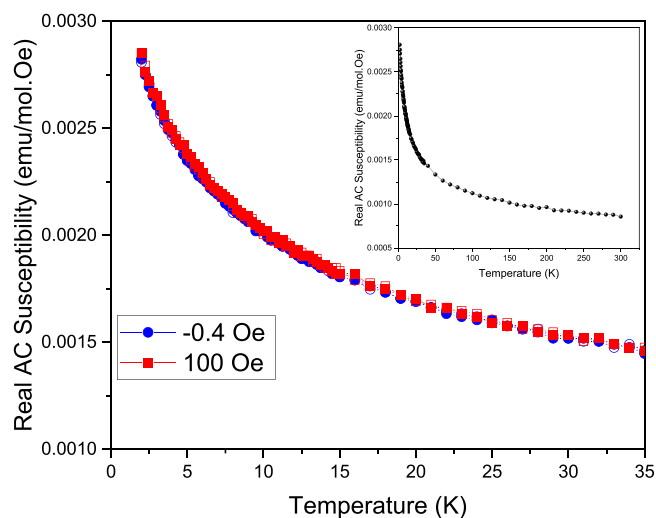
paramagnetic response, transformed to a spin glass behaviour at 6 K. Overall, our results highlight the potential of the cold-sintering method as a benign, facile method for densifying Na-ion compounds.
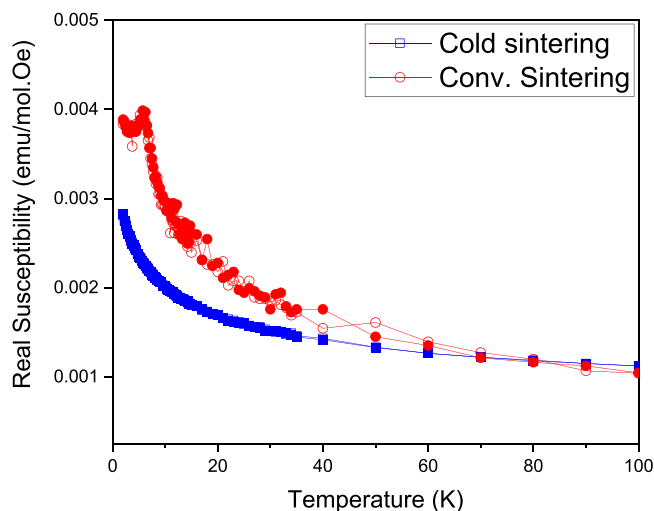
Fig. 14. Real ac susceptibility (consistent with Fig. 13) as a function of temperature at zero applied fields for an ac frequency of 757 Hz for conventional and cold sintered NCO. Solid and open symbols correspond to heating and cooling, respectively.
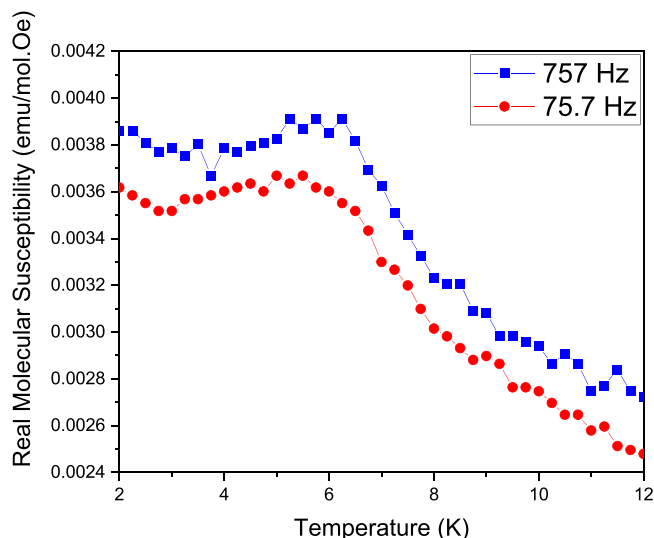

Fig. 15. Real susceptibility as a function of temperature and ac frequency at zero applied fields for the conventionally sintered NCO.

CRediT authorship contribution statement

Ian M. Reaney: Writing – review & editing, Writing – original draft, Visualization, Validation, Supervision, Project administration, Methodology, Investigation, Formal analysis, Data curation, Conceptualization. **Derek C. Sinclair:** Writing – review & editing, Writing – original draft, Visualization, Validation, Investigation, Data curation. **Oday Hussein:** Validation, Data curation. **Nicola Morley:** Writing – review & editing, Writing – original draft, Validation, Supervision, Data curation. **Brant Walkley:** Writing – review & editing, Validation, Supervision. **Beatia In Siame:** Validation, Methodology. **Igor Levin:** Writing – review & editing, Writing – original draft, Validation, Supervision, Methodology, Investigation, Formal analysis, Data curation. **Ademola Joseph Adetona:** Writing – review & editing, Writing – original draft, Visualization, Validation, Project administration, Methodology, Investigation, Funding acquisition, Formal analysis, Data curation, Conceptualization.

Declaration and Conflict of Interest

The authors declare no known competing financial interests that could have influenced the work reported in this paper.

Appendix A. Supporting information

Supplementary data associated with this article can be found in the online version at doi:10.1016/j.jeurceramsoc.2024.116792.

References

[1] C. Delmas, J. Braconnier, C. Fouassier, P. Hagenmuller, Electrochemical intercalation of sodium in Na_xCoO_2 bronzes, Solid State Ion. vol. 3–4 (Aug. 1981) 165–169, https://doi.org/10.1016/0167-2738(81)90076-x.

[2] M. Blangero, D. Carlier, M. Pollet, J. Darriet, C. Delmas, Jean-Pierre Doumerc, High-temperature phase transition in the three-layered sodium cobaltite P'3-Na_xCoO_2 (x~,", Phys. Rev. B vol. 77 (18) (May 2008) https://doi.org/10.1103/physrevb.77.184116.

[3] C. Oopathump, D. Boonthuma, S. Meejoo Smith, Effect of poly(Vinyl Alcohol) on thermoelectric properties of sodium cobalt oxide, Key Eng. Mater. (Apr. 2019), https://doi.org/10.4028/www.scientific.net/kem.798.304.

[4] R.V. Narayan, V. Kanniah, A. Dhathathreyan, Tuning size and catalytic activity of nano-clusters of cobalt oxide, J. Chem. Sci. vol. 118 (2) (Mar. 2006) 179–184, https://doi.org/10.1007/bf02708470.

[5] Y. Sassa, I. Umegaki, H. Nozaki, O.K. Forslund, C. Delmas, J.C. Orain, A. Amato, D. Andreica, M. Månsson, J. Sugiyama, Investigation of the magnetic properties of $Na_{0.7}CoO_2$ prepared by electrochemical reaction, DORA PSI (Paul. Scherrer Inst. (2018), https://doi.org/10.7566/jpscp.21.011019.

[6] K. Takada, H. Sakurai, E. Takayama-Muromachi, F. Izumi, R.A. Dilanian, T. Sasaki, Superconductivity of a hydrous sodium cobalt oxide, Phys. C: Supercond. vol. 408–410 (Aug. 2004) 165–168, https://doi.org/10.1016/j.physc.2004.02.068.

[7] K. Ishida, Y. Ihara, Y. Maeno, C. Michioka, M. Kato, K. Yoshimura, K. Takada, T. Sasaki, H. Sakurai, E. Takayama-Muromachi, Unconventional superconductivity and nearly ferromagnetic spin fluctuations in $Na_xCoO_2 \cdot yH_2O$, J. Phys. Soc. Jpn. 72 (2003) 3041–3044, doi.org/10.1143/jpsj.72.3041.

[8] H.D. Yang, J.-Y. Lin, C.P. Sun, Y.C. Kang, C.L. Huang, K. Takada, T. Sasaki, H. Sakurai, E. Takayama-Muromachi, Evidence of nodal superconductivity in $Na_{0.35}CoO_2 \cdot 1.3H_2O$: a specific-heat study, Phys. Rev. B 71 (2005), https://doi.org/10.1103/physrevb.71.020504.

[9] J.W. Lynn, Q. Huang, C.M. Brown, V.L. Miller, M.L. Foo, R.E. Schaak, C.Y. Jones, E. A. Mackey, R.J. Cava, Structure and dynamics of superconducting Na_xCoO_2 hydrate and its unhydrated analogue, Phys. Rev. B 68 (2003), https://doi.org/10.1103/physrevb.68.214516.

[10] Y. Lei, X. Li, L. Liu, G. Ceder, Synthesis and stoichiometry of different layered sodium cobalt oxides, Chem. Mater. vol. 26 (18) (Sep. 2014) 5288–5296, https://doi.org/10.1021/cm5021788.

[11] M. Miclau, Kiran Kumar, Bokinala, Nicolae Miclau, Low-temperature hydrothermal synthesis of the three-layered sodium cobaltite P3-Na_xCoO_2 (x~0.60), Mater. Res. Bull. vol. 54 (Jun. 2014) 1–5, https://doi.org/10.1016/j.materresbull.2014.02.018.

[12] H. Wang, J. Wu, Andrei Dolocan, Y. Li, Xujie Lü, N. Wu, K. Park, S. Xin, M. Lei, W. Yang, J.B. Goodenough, Short O–O separation in layered oxide $Na_{0.67}CoO_2$ enables an ultrafast oxygen evolution reaction, Proc. Natl. Acad. Sci. USA 116 (2019) 23473–23479, https://doi.org/10.1073/pnas.1901046116.

[13] H. Kähäri, M. Teirikangas, J. Juuti, H. Jantunen, Dielectric properties of lithium molybdate ceramic fabricated at room temperature, J. Am. Ceram. Soc. vol. 97 (11) (Oct. 2014) doi.org/10.1111/jace.13277.

[14] H. Guo, A. Baker, J. Guo, C.A. Randall, Cold sintering process: a novel technique for low-temperature ceramic processing of ferroelectrics, J. Am. Ceram. Soc. vol. 99 (11) (Oct. 2016) 3489–3507, https://doi.org/10.1111/jace.14554.

[15] Z.A. Grady, Z. Hugh Fan, Arnaud Ndayishimiye, C.A. Randall, Design and sintering of all-solid-state composite cathodes with tunable mixed conduction properties via the cold sintering process, ACS Appl. Mater. Interfaces 13 (2021) 48071–48087, https://doi.org/10.1021/acsami.1c13913.

[16] J. Guo, H. Guo, A.L. Baker, M.T. Lanagan, E.R. Kupp, G.L. Messing, C.A. Randall, Cold sintering: a paradigm shift for processing and integration of ceramics, Angew. Chem. 128 (2016) 11629–11633, https://doi.org/10.1002/ange.201605443.

[17] Z.A. Grady, K. Tsuji, A. Ndayishimiye, J.H. Seo, C.A. Randall, Densification of a solid-state NASICON sodium-ion electrolyte below 400C by cold sintering with a fused hydroxide solvent, ACS Appl. Energy Mater. 3 (2020) 4356–4366, https://doi.org/10.1021/acsaem.0c00047.

[18] S.S. Faouri, A. Mostaed, J.S. Dean, D. Wang, D.C. Sinclair, S. Zhang, W.G. Whittow, Y. Vardaxoglou, I.M. Reaney, High-quality factor cold sintered $Li_2MoO_4BaFe_{12}O_{19}$ composites for microwave applications, Acta Mater. 166 (2019) 202–207, https://doi.org/10.1016/j.actamat.2018.12.057.

[19] D. Wang, B. Siame, S. Zhang, G. Wang, X. Ju, J. Li, Z. Lu, Y. Vardaxoglou, W. Whittow, D. Cadman, S. Sun, D. Zhou, K. Song, I.M. Reaney, Direct integration of cold sintered, temperature-stable $Bi_2Mo_2O_9$-K_2MoO_4 ceramics on printed circuit boards for satellite navigation antennas, J. Eur. Ceram. Soc. 40 (2020) 4029–4034, https://doi.org/10.1016/j.jeurceramsoc.2020.04.025.

[20] J. Andrews, D. Button, I.M. Reaney, Advances in Cold Sintering: improving energy consumption unlocking new potential in component manufacturing, Johns. Matthey Technol. Rev. vol. 64 (2) (Apr. 2020) 219–232, https://doi.org/10.1595/205651320X15814150061554.

[21] L. Li, J. Andrews, R. Mitchell, D. Button, D.C. Sinclair, I.M. Reaney, Aqueous cold sintering of Li-based compounds, ACS Appl. Mater. Interfaces vol. 15 (16) (Apr. 2023) 20228–20239, https://doi.org/10.1021/acsami.3c00392.

[22] A.J. Adetona *"Densification of Na-ion compounds by conventional and cold-sintering.* ⟨https://etheses.whiterose.ac.uk/id/oai_id/oai:etheses.whiterose.ac.uk:34437⟩.

[23] J.-H. Seo, H. Nakaya, Y. Takeuchi, Z. Fan, H. Hikosaka, R. Rajagopalan, E. D. Gomez, M. Iwasaki, C.A. Randall, Broad temperature dependence, high conductivity, and structure-property relations of cold sintering of LLZO-based composite electrolytes, J. Eur. Ceram. Soc. 40 (2020) 6241–6248, https://doi.org/10.1016/j.jeurcera.

[24] A. Galotta, V.M. Sglavo, The cold sintering process: a review on processing features, densification mechanisms and perspectives, J. Eur. Ceram. Soc. vol. 41 (16) (Dec. 2021) 1–17, https://doi.org/10.1016/j.jeurceramsoc.2021.09.024.

[25] C. Vakifahmetoglu, L. Karacasulu, Cold sintering of ceramics and glasses: a review, Curr. Opin. Solid State Mater. Sci. vol. 24 (1) (Feb. 2020) 100807, https://doi.org/10.1016/j.cossms.2020.100807.

[26] R. Aso, T. Katsumata, T. Nakamura, Yusuke Watase, Koji Amezawa, and Y. Murakami, "Structural, electronic characterisation of fluorine-doped $La_{0.5}Sr_{0.5}CoO_{3-\delta}$ using electron energy-loss spectroscopy," May 2023, https://doi.org/10.1093/jmicro/dfad031.

[27] L. Li, J. Andrews, R. Mitchell, D. Button, D.C. Sinclair, I.M. Reaney, Aqueous cold sintering of Li-based compounds, ACS Appl. Mater. Interfaces 15 (16) (2023) 20228–20239, https://doi.org/10.1021/acsami.3c00392.

[28] S. Funahashi, J. Guo, H. Guo, K. Wang, A.L. Baker, K. Shiratsuyu, C.A. Randall, Demonstration of the cold sintering process study for the densification and grain growth of ZnO ceramics, J. Am. Ceram. Soc. 100 (2) (2016) 546–553, https://doi.org/10.1111/jace.14617.

[29] L. Xue, X. Shi, B. Lin, Q. Guo, Y. Zhao, H. Xia, Self-standing P2/P3 hetero-structured $Na_{0.7}CoO_2$ nano-sheet arrays as 3D cathodes for flexible sodium-ion batteries, 457 (2020) 228059–228059. doi.org/10.1016/j.jpowsour.2020.228059.

[30] M. Medarde, M. Mena, J.L. Gavilano, E. Pomjakushina, J. Sugiyama, K. Kamazawa, V. Pomjakushin, D. Sheptyakov, B. Batlogg, H.R. Ott, M. Mansson, F. Jurányi, 1D to 2D Na^+ ion diffusion inherently linked to structural transitions in $Na_{0.7}CoO_2$, Phys. Rev. Lett. 110 (2013), https://doi.org/10.1103/physrevlett.110.266401.

[31] H.W. Zandbergen, M.L. Foo, Q. Xu, V. Kumar, R.J. Cava, Na-ion ordering in Na_xCoO_2: electron diffraction study vol. 70 (2) (Jul. 2004), https://doi.org/10.1103/physrevb.70.024101.

[32] F. Huang, M.W. Chu, G.J. Shu, H.S. Sheu, C.H. Chen, L.K. Liu, P.A. Lee and F.C. Chou, "X-ray and electron diffraction studies of superlattices and long-range three-dimensional Na ordering in γ-Na_xCoO_2 (x = 0.71 and 0.84)," vol. 79, no. 1, Jan. 2009, https://doi.org/10.1103/physrevb.79.014413.

[33] O.A. Makgae, T.N. Phaahlamohlaka, B. Yao, M.E. Schuster, T.J.A. Slater, P. P. Edwards, N.J. Coville, E. Liberti, A.I. Kirkland, Atomic structure and valence state of Cobalt nanocrystals on Carbon under syngas versus Hydrogen reduction, J. Phys. Chem. C. 126 (2022) 6325–6333, https://doi.org/10.1021/acs.jpcc.2c00482.

[34] S. Hwang, Y. Lee, E. Jo, Kyung Yoon Chung, W. Choi, Seung Min Kim, W. Chang, Investigation of thermal stability of P2–Na_xCoO_2 cathode materials for sodium-ion batteries using real-time electron microscopy, ACS Appl. Mater. Interfaces 9 (2017) 18883–18888, https://doi.org/10.1021/acsami.7b04478.